International Journal of Biological Macromolecules 158 (2020) 420–429

Contents lists available at ScienceDirect

International Journal of Biological Macromolecules

journal homepage: http://www.elsevier.com/locate/ijbiomac

Structure and properties of thermomechanically processed chitosan/carboxymethyl cellulose/graphene oxide polyelectrolyte complexed bionanocomposites

Pei Chen [a,b], Fengwei Xie [b,c,*,1], Fengzai Tang [d], Tony McNally [b,**]

[a] College of Food Science, South China Agricultural University, Guangzhou, Guangdong 510642, China
[b] International Institute for Nanocomposites Manufacturing (IINM), WMG, University of Warwick, Coventry CV4 7AL, United Kingdom
[c] School of Chemical Engineering, The University of Queensland, Brisbane, QLD 4072, Australia
[d] WMG, University of Warwick, Coventry CV4 7AL, United Kingdom

ARTICLE INFO

Article history:
Received 24 March 2020
Received in revised form 23 April 2020
Accepted 29 April 2020
Available online 3 May 2020

Keywords:
Polysaccharide
Thermomechanical processing
Polyelectrolyte complexation
Graphene oxide
Microstructure
Contact angle

ABSTRACT

Bionanocomposites of chitosan and chitosan/carboxymethyl cellulose (CMC) polyelectrolyte complexed materials with graphene oxide (GO) or reduced graphene oxide (rGO) were prepared by thermomechanical processing with excellent levels of dispersion. While GO has a greater affinity with the chitosan polycation, rGO had a more pronounced effect on properties resulting in increased tensile strength, Shore D hardness, and thermal stability of both matrices. Although GO is more hydrophilic than rGO, the former increased more effectively the surface hydrophobicity of the biocomposites regardless of matrix type. GO and rGO changed the α-transition of the biocomposites in a similar manner. The electrochemical properties of the biocomposites were influenced by both nanofiller type and matrix. This research revealed that inclusion of 2D carbon nanomaterials can alter biopolymer interactions and that the phase structure of the biopolymer blend may play a more important role than nanofiller–matrix interactions in determining the overall properties of these bionanocomposites.

1. Introduction

Compared to traditional synthetic polymers, natural biopolymers such as cellulose, chitin, starch and protein have many advantages such as renewability, wide availability, biodegradability, nontoxicity, and biocompatibility. Moreover, biopolymers present natural functionality (*e.g.* antimicrobial activity of chitosan) and have multiple reactive sites (*e.g.* hydroxyl and amine groups) for chemical derivatisation and the introduction of additional novel functional groups. Hence, there has been tremendous interest in biopolymers for advanced materials for diverse applications including, biomedical (*e.g.* drug delivery, tissue engineering, implants, patches, and 3D printed organs) [1–6], antimicrobial packaging and coating [7,8], fuel cells [9], oil/water separation [10,11], solar water purification [12], ionic conductive membranes [13], smart textiles and soft robotics [14], and for tribological power generation [15].

Furthermore, various synthetic nanomaterials (*e.g.*, graphene, carbon nanotubes, mineral nanoparticles and metallic nanoparticles) can be efficiently integrated into biopolymers to achieve novel properties such as superior electrical and thermal conductivity, controlled gas barrier properties, complex actuation, and unique optical properties [16]. Among different nanomaterials, graphene in the form of 2D nanosheets has attracted the most attention because of its high thermal conductivity, superior mechanical properties and excellent electronic transport properties [17]. Interestingly, the antimicrobial activity of graphenic nanomaterials has also been demonstrated [18–21]. There have been many studies on composites of biopolymers and graphene, which have shown advantageous properties and appealing functionality. For example, conductive hydrogels based on chitosan and graphene were developed with excellent tuneable swelling properties and biocompatibility [22]. A robust and soft antimicrobial hydrogel biofilm was fabricated based on chitosan and iron oxide-coated graphene oxide (GO) [23]. Composites of chitosan and graphene showed improved hydrothermal and chemical stability [24]. The addition of GO to chitosan could enhance mechanical properties and tailor the drug-release behaviour and biodegradation [25]. Similarly, chitosan/carboxymethyl cellulose (CMC)/GO aerogels were developed for pH-controlled drug delivery [26].

On the other hand, polyelectrolyte complexation (PEC) has been an interesting topic as it opens the possibility of creating responsive and

* Correspondence to: F. Xie, International Institute for Nanocomposites Manufacturing (IINM), WMG, University of Warwick, Coventry CV4 7AL, United Kingdom.
** Corresponding author.
E-mail addresses: d.xie.2@warwick.ac.uk (F. Xie), t.mcnally@warwick.ac.uk (T. McNally).
[1] This author leads the research.

https://doi.org/10.1016/j.ijbiomac.2020.04.259
0141-8130/

smart materials with tailored strength or texture based on the dissociation/reassociation of oppositely charged polymer chains [27,28]. The concept of PEC has been applied to create biopolymer materials for various applications. For example, chitosan/alginate scaffolds showed both satisfactory mechanical properties [29] and cell adhesiveness [30]. Chitosan/CMC coatings displayed outstanding barrier properties [31]. Applying PEC, lignin was used as an underwater adhesive with excellent strength [32]. Our recent research has led to the creation of chitosan/carboxymethyl cellulose (CMC) films by PEC, with unexpectedly higher water-resistance than either biological component alone [33].

In this work, different chitosan and chitosan/CMC polyelectrolyte complexed materials containing either GO or rGO were prepared by thermomechanical processing. This "dry" method has been shown to be cost-effective for processing biopolymers [33–36] but has scarcely been reported for the preparation of composites of biopolymers and graphene. The strong shear effect during the thermomechanical processing of high-viscosity materials is expected to facilitate the disruption of the original hydrogen-bonding network, the dispersion of the nanomaterials in the matrices, and the interactions between biopolymer chains and between different components. This makes thermomechanical processing more advantageous than widely used solution methods for preparing biopolymer nanocomposites. We propose that the structure and properties of thermomechanically processed dual-biopolymer-based nanocomposites are not predominantly determined by the chemistry of the 2D carbon nanomaterial. In this study, we discuss multiple factors in such nanocomposite systems that are key in determining the composite material structure and properties providing insights into the design of novel bionanocomposites.

2. Experimental

2.1. Materials

Chitosan (poly(β-(1,4)-D-glucosamine), derived from crustaceous shells, was purchased from Shanghai Ryon Biological Technology Co., Ltd. (China). This chitosan has a molecular weight of about 150,000 $g \cdot mol^{-1}$, a degree of deacetylation of >90%, and a viscosity of about 100 mPa·s (*i.e.* 1% solution in 1% acetic acid at 25 °C). This chitosan was characterised previously [37]. Carboxymethyl cellulose (CMC) sodium, with a molecular mass of 90,000 $g \cdot mol^{-1}$, a degree of substitution (DS) of 0.7, and a viscosity of 50–100 mPa·s (Brookfield, 2% solution, at 25 °C), was purchased from Shanghai Macklin Biochemical Co., Ltd. (China). The characteristics of this CMC are shown in our previous study [33]. Graphene oxide, in the form of an aqueous acid paste (25% GO, 74% water, and 1–1.5% HCl), was purchased from Abalonyx AS (Oslo, Norway). Hydrazine hydrate solution (78–82% iodometric, Honeywell Fluka) and ammonia solution (35%, AR, d = 0.88) were supplied by Fisher Scientific UK Ltd. (Loughborough, UK); formic acid (98% w/w AR) and NaBr (pure) by Scientific Laboratory Supplies Ltd. (Nottingham, UK). Deionised water was used.

2.2. Synthesis of reduced graphene oxide (rGO)

Reduced graphene oxide (rGO) was prepared from graphene oxide (GO) following the procedure of Abbas, Rees, Kelly, Dancer, Hanna and McNally [38]. Briefly, 40 g of the GO paste (25 wt% concentration) with 150 mL distilled water was added to a round-bottom flask, which was further added with a mixture of 25 mL of the hydrazine hydrate solution and 25 mL of the ammonia solution (both used as received). The mixture was heated at 90 °C for 4 h with magnetic stirring under reflux. This mixture was filtered and washed with water to reach neutral pH, followed by drying in a vacuum oven. For the powder product obtained, the same procedure was undertaken once again to ensure adequate reaction.

2.3. Sample preparation

Table 1 shows the formulations and codes of different samples prepared. In the codes, "A" means the matrix with only chitosan while "B" indicates chitosan/CMC mix. The sample preparation was described previously [33] including pre-blending with 2 M formic acid solution, thermomechanical kneading at 80 °C for 15 min, hot-pressing at 110 °C and 160 bar for 10 min, and conditioning at 57% relative humidity (RH) for 3 weeks; The GO and rGO suspensions (dispersed in 2 M formic acid and sonicated at 200 W and, 24 kHz for 10 min) were added during the pre-blending stage. The controls A-F and B-F were characterised previously [33] with the exception of their electrochemical properties.

2.4. Sample characterisation

X-ray photoelectron Spectroscopy (XPS) was carried out using a Kratos Axis Ultra DLD Spectrometer at room temperature and with a base pressure of 2×10^{-10} mbar, using a monochromated Al Kα X-ray source. To prevent surface charging the data was collected while the sample was, exposed to a flux of low energy electrons from the charge neutraliser built in to the hemispherical analyser entrance, with the binding energy scale retrospectively calibrated to the sp^3 C—C peak at 284.6 eV. The data was analysed with the CasaXPS software package, using Shirley backgrounds and mixed Gaussian–Lorentzian (Voigt) line shapes and asymmetry parameters where appropriate. For compositional analysis, the analyser transmission function was determined using clean metallic foils to determine the detection efficiency across the full binding energy range.

Scanning electron microscopy (SEM) imaging was performed using a Zeiss Sigma field-emission gun microscope (Carl Zeiss AG, Oberkochen, Germany) with an acceleration voltage of 6 kV. The films were cryo-fractured using liquid nitrogen and sputter-coated with gold/palladium.

Transmission electron microscopy (TEM) was conducted using a Talos F200X microscope (Thermo Fisher Scientific, Waltham, MA, USA) at 200 kV. Both high-angle annular dark-field (HAADF) and bright field (BF) images were acquired simultaneously in the scanning TEM (STEM) mode, while electron diffraction analysis was performed in the conventional TEM mode. For STEM imaging of pure GO and rGO, the carbon nanomaterials were dispersed in water at 0.01 wt% concentration and sonicated for 10 min, before being deposited onto holey carbon films on 200-mesh copper grids and dried at 40 °C. For the STEM imaging of the bionanocomposites, ribbons about 60 nm thick were sectioned from epoxy-embedded sample blocks and subsequently transferred onto the same type of grids, during which no liquid was involved to avoid damage to the samples.

X-ray diffraction (XRD) patterns were acquired using a PANalytical Empyrean X-ray diffractometer (Malvern Panalytical Ltd., Malvern, UK) with a Co target (Kα = 1.790307 Å), a PIXcel1D (RTMS type) detector, and a beam slit of 10 mm at 40 kV and 40 mA. The samples were scanned over an angular range (2θ) of 6–40° with a step size of 0.0263° and a step rate of 2.16 s/step.

Attenuated total reflection Fourier-transform infrared (ATR-FTIR) spectra were recorded at room temperature (RT) using a Bruker

Table 1
Sample codes and material compositions (represented as portions by weight).

Sample	Chitosan	CMC	GO	rGO	2 M formic acid
A-F[a]	100	–	–	–	260.67
A/GO-F	100	–	0.75	–	260.67
A/rGO-F	100	–	–	0.75	260.67
B-F[a]	50	50	–	–	260.67
B/GO-F	50	50	0.75	–	260.67
B/rGO-F	50	50	–	0.75	260.67

[a] Partly reported in our previous work [33].

TENSOR 27 FTIR spectrometer (Bruker Corporation, Billerica, MA, USA) with 32 scans for each sample over the range of 4000–500 cm^{-1}.

Dynamic mechanical thermal analysis (DMTA) was undertaken using a Tritec 2000 DMA facility (Triton Technology Ltd., Nottinghamshire, UK) in the dual cantilever mode with a sample length of 5 mm at 0.01 mm displacement. Temperature scans were performed from −100 °C to 180 °C at 2 K/min and a frequency of 1 Hz.

Tensile tests were conducted using an Instron 3367 universal testing machine (Norwood, MA, USA) with a 1kN load cell at a crosshead speed of 3 mm/min. As the specimens were in the form of thin sheets, specimen extension was measured by grip separation as suggested by ASTM Standard D882. At least seven replicates were tested for each composite sample.

Share D Hardness was measured using a hardness tester (HT 3000 Auto, MonTech Rubber Testing Solutions, Buchen, Germany) according to ASTM D2240 Standard.

Thermo-gravimetric analysis (TGA) was performed using a Mettler Toledo TGA (Mettler Toledo, Columbus, OH, USA) over a temperature range of 30–700 °C at 10 K/min under nitrogen.

Contact angle (θ_c) data were collected from sessile tests at RT based on Young–Laplace using an Attension Theta Lite instrument (Biolin Scientific, Manchester, UK).

Electrochemical impedance spectroscopy (EIS) was performed using a Princeton Applied Research PARSTAT MC (PMC) multi-channel potentiostat (Ametek Scientific Instruments, Berwyn, PA, USA) with a PMC-2000 card and a two-point probe. The two surfaces of samples were painted with carbon conductive grease (No.8481, MG Chemicals, Surrey, B.C., Canada) in designated areas (24 × 24 mm). The measurements were made in at least triplicate for each sample. The real (Z') and imaginary (Z'') parts of impedance and phase angle (θ) between current and voltage were evaluated with a frequency (f) range between 1 Hz and 1 M Hz. The AC conductivity (admittance) (σ), the real (ε'_r) and imaginary (ε''_r) parts of relative permittivity, the real (M') and imaginary (M'') parts of electric modulus, and dielectric loss tangent ($\tan\delta$) were calculated using the following equations, [39–41]:

$$\sigma = \frac{Z\prime}{Z\prime^2 + Z''^2} \cdot \frac{t}{A} \tag{1}$$

$$\varepsilon\prime_r = \frac{-Z''}{Z\prime^2 + Z''^2} \cdot \frac{t}{\omega A \varepsilon_0} \tag{2}$$

$$\varepsilon''_r = \frac{Z\prime}{Z\prime^2 + Z''^2} \cdot \frac{t}{\omega A \varepsilon_0} \tag{3}$$

$$M\prime = \frac{\varepsilon\prime}{\varepsilon\prime^2 + \varepsilon''^2} \tag{4}$$

$$M'' = \frac{\varepsilon''}{\varepsilon\prime^2 + \varepsilon''^2} \tag{5}$$

$$tan\delta = \frac{Z\prime}{-Z''} \tag{6}$$

Here, ω is the angular frequency ($=2\pi f$), ε_0 is the permittivity of free space ($\approx 8.854 \times 10^{-12}\ F \cdot m^{-1}$), A is the tested area of the sample (m^2), and t is the sample thickness (m).

The bulk resistance (R_b) was determined from the Nyquist plots of impedance (Z'' *vs.* Z') either from the intercept of the semicircle of the real (Z') axis, if only semicircular parts are seen or from the points where the semicircle and the straight line meet. Then, the DC conductivity (σ_{dc}) can be calculated using Eq. (7) [39,42]:

$$\sigma_{dc} = \frac{t}{R_b \cdot A} \tag{7}$$

3. Results and discussion

3.1. Characterisation of GO and rGO

Fig. S1 shows the FTIR spectra for GO and rGO. While pure graphene is IR-inactive, GO displayed a wide band in the range of 2872–3692 cm^{-1}, associated with O—H stretching and hydrogen bonding. Besides, GO also showed FTIR peaks at 1724 cm^{-1} and 1042 cm^{-1}, corresponding to carbonyl (C═O stretching) and epoxy (C—O—C) groups, respectively. The peak at 1618 cm^{-1} could be due to an overlap of the signals for O—H deformation and C═C aromatic vibration. For rGO, these characteristic bands disappeared, indicating successful chemical reduction of GO.

Further evidence for reduction of GO was obtained from X-ray photoelectron spectroscopy (XPS). Table S1 shows the total element percentages for GO and rGO, corresponding to the intensity changes in the survey spectra (Fig. S2a and b). Compared with those of GO, rGO showed a significantly reduced oxygen ratio (from 34.3% to 9.0%) accompanied by a higher carbon content (from 63.3% to 88.3%), suggesting successful reduction, *i.e.* an increase in sp^2 hybridisation and a reduction in sp^3 hybridisation. Fig. S1c–f shows the deconvoluted C_{1s} and O_{1s} spectra for GO and rGO and related data are listed in Table S2. Compared with GO, rGO showed significantly increased peak intensities for sp^3 C—C bond (284.8 eV) and graphene (284.5 eV) and largely suppressed peaks for C—O (286.2 eV), C═O (287.5 eV), O═C—O (288.7 eV), and organic oxygen (533.5 eV), further confirmation of the effective chemical reduction of GO to rGO.

Fig. S3a shows STEM images of GO and rGO. GO was ultrasonically exfoliated into some individual nanosheets. For rGO under the same ultrasonication treatment, the stacking of exfoliated nanosheets was apparent [43]. rGO showed a clear diffraction pattern, from which a *d*-spacing of rGO was calculated to be 0.41 nm in agreement with previous work [44].

3.2. Morphology

Fig. S4 shows the SEM images of cryo-fractured surfaces of different biocomposite films. All the samples displayed a cohesive surface morphology without the original clumpy features of chitosan [37] and CMC [33], indicating successful processing of the biopolymers. The samples with GO and rGO did not show any significant difference in morphology at the magnification shown. Compared with A-F, A/GO-F and A/rGO-F seemed to have a more cohesive structure, which might be contributed by the addition of the 2D carbon nanomaterials.

The extent of GO or rGO dispersion in the biopolymers was examined by STEM, see Fig. 1. While A/GO-F and A/rGO-F reveal structural features of chitosan, the darker colour in the BF images (or the brighter colour in HAADF images), also exhibited by A-F [33], additional flocculent or cloudy substances (indicated by the arrows) could be seen, which can be ascribed to GO or rGO. Clearly, the GO/rGO were partially exfoliated and adequately dispersed in the chitosan matrix such that they appeared at low light contrast under STEM imaging, (see arrows in Fig. 1. Excellent dispersion of GO in chitosan materials has been demonstrated before [45–47]. It has been suggested that the oxygen-containing groups (*e.g.* —COOH and —OH) and negative charges as a result of ionisation of carboxylic acid and phenolic hydroxyl groups on the GO nanosheets can interact effectively with the polycationic chitosan through hydrogen bonding and electrostatic attraction [45]. Although rGO is less hydrophilic and less negatively charged than GO, notable dispersion of rGO was still observed, which may be a consequence of the thermomechanical treatment of the high-viscosity chitosan system.

Similarly, the shear stress applied during mechanical mixing plays a major role in the dispersion of rGO in the chitosan/CMC matrix, as in B/rGO-F where the rGO was well dispersed. However, in the same matrix (B/GO-F), more large agglomerates could be seen, suggesting the GO nanosheets re-aggregate. In this case, the strong interactions between

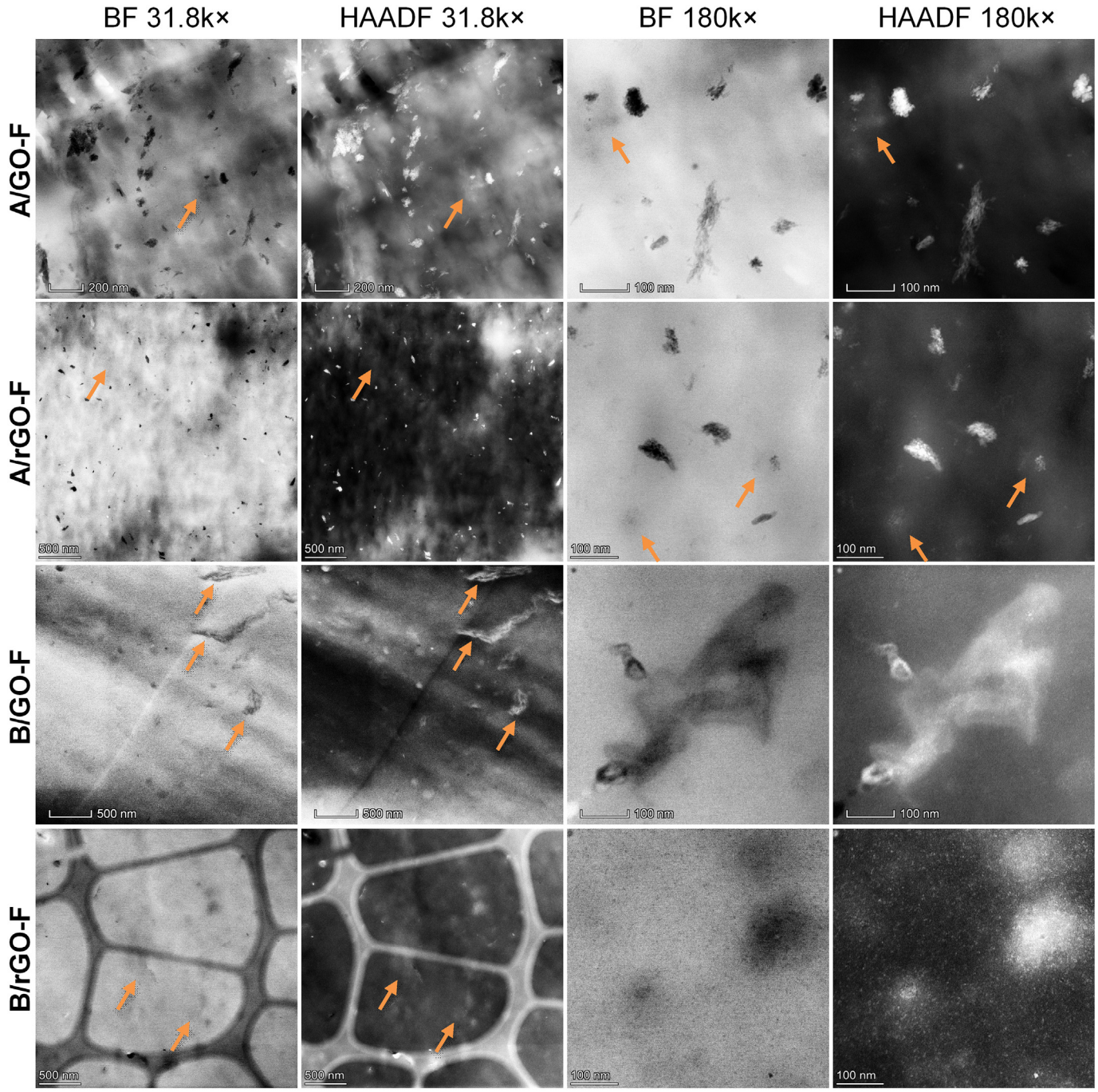

Fig. 1. STEM images of the different bionanocomposite films. BF, bright field; HAADF, high-angle annular dark-field. The arrows indicate GO or rGO.

reversely charged chitosan and CMC and the negative charge of CMC might have hindered the dispersion of GO.

3.3. Crystalline structure

The crystalline structures of the different bionanocomposite films were studied using XRD, see Fig. 2. A/GO-F and A/rGO-F showed similar XRD patterns as that for A-F [33]. As the XRD patterns for these films are completely different from that for unprocessed chitosan [37], the processing should have destroyed the original crystalline structure of chitosan and led to the formation of a new crystalline structure. The intensity of the peaks for A/GO-F and A/rGO-F were less than those for A-F, suggesting the addition of GO or rGO might have limited re-crystallisation. Moreover, A/rGO-F shows slightly stronger XRD peak intensities than A/GO-F. In this regard, chitosan has less hydrogen-bonding and electrostatic interactions with rGO than with GO, so re-crystallisation could be less restricted in A/rGO-F.

For the B-series of biopolymer films, the characteristic reflections of unprocessed CMC are absent [33]. Similar to B-F [33], B/rGO-F only showed slight reflections at 13.5° and 30.8° 2θ characteristic of the processed chitosan. B/GO-F was totally amorphous. Apparently, both the interactions between CMC and chitosan and the addition of GO restricted chitosan chain movement and thus re-crystallisation.

3.4. Molecular interactions

ATR-FTIR was used to detect chemical interactions in the different bionanocomposite films, see spectra shown in Fig. 3. Both A/GO-F and

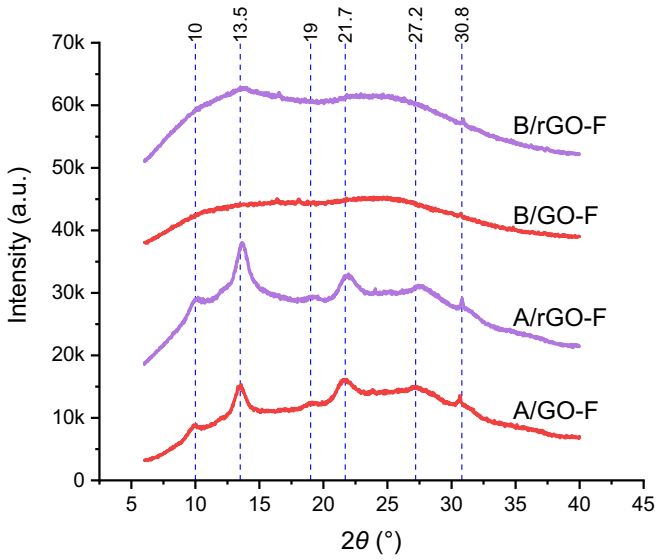

Fig. 2. X-ray diffractograms for the different bionanocomposite films. The references lines indicate the characteristic peaks of A-F.

A/rGO-F displayed quite similar FTIR spectra as that for unprocessed chitosan [37] or for A-F [33]. This implies that the thermomechanical processing and the addition of GO or rGO did not disrupt the chemical interactions in chitosan, as expected. For A/GO-F, shifts in the band positions at 1256 cm^{-1} (Amide III), 1065 cm^{-1} (asymmetric C—O—C stretching in glycosidic linkage) and 1022 cm^{-1} (skeletal vibration of C—O stretching) [48–50] could be seen (indicated by arrows). The changes should be caused by the interaction of GO with chitosan.

The FTIR spectra for the B-series of films were similar to those for the A-series of formulations. There was an additional reflection at 1414 cm^{-1} due to the asymmetric stretching vibration of carboxylate ions [51–54]. Furthermore, a blue-shift in the band position at 1572 cm^{-1} (N—H bending from amine and amide II) and a red-shift in the band position at 1065 cm^{-1} (asymmetric C—O—C stretching in glycosidic linkage) [48–50] could be noticed, signifying strong molecular interactions between the two biopolymers. No apparent difference in the FTIR spectrum between B/GO-F and B/rGO-F could be observed,

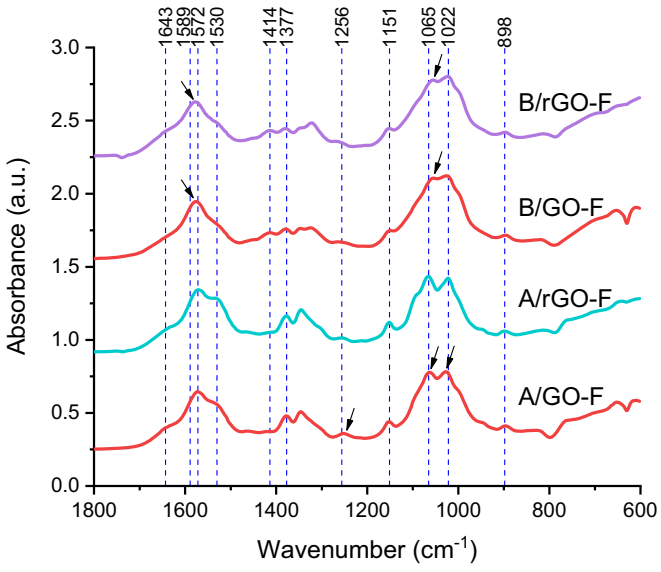

Fig. 3. FTIR spectra for the different bionanocomposite films. The reference lines indicate characteristic bands of unprocessed CMC (1589 and 1414 cm^{-1}) [33] and chitosan (the rest) [33]. The arrows indicate shifts in peak position.

suggesting again, the addition of GO or rGO did not result in any changes to the chemical interactions in the biopolymers.

3.5. Molecular relaxations

The molecular relaxation of the bionanocomposite films was studied by DMTA with the loss tangent (tan δ) plots as a function of temperature shown in Fig. 4. A/GO-F and A/rGO-F showed very similar tan δ profiles as that for A-F, with a β-relaxation at a lower temperature and an α-transition (glass transition) at a higher temperature [33]. For these two samples, the α-transition temperature was unchanged. Nevertheless, an increase in the β-relaxation peak temperature (*i.e.* −34 °C for A/GO-F and −45 °C for A/rGO-F compared with −47 °C for A-F) was attained. In this regard, the interactions between chitosan chains and GO/rGO could have limited the mobility of the side chains or lateral groups of chitosan [55,56], with GO being more effective due to its greater hydrogen-bonding and electrostatic interactions with chitosan chains.

B-F also exhibited two major transitions (the β-transition centre at −43 °C and the α-transition at 97 °C) [33]. In comparison, B/GO-F and B/rGO-F displayed an increased β-transition peak temperature (−24 °C and −25 °C) and α-transition peak temperature (120 °C and 121 °C). In this case, despite the complexation between chitosan and CMC, GO or rGO was still capable of restricting biopolymer chain movement, resulting in a higher α-transition temperature. For B/GO-F, there may be some interactions between chitosan chains and GO. However, the similar α-transition peak temperatures for B/GO-F and B/rGO-F demonstrates that the constrained mobility of the main biopolymer chains provided by well-dispersed GO or rGO was likely to be mainly due to a steric hindrance effect but much less from contributions from hydrogen-bonding and electrostatic interactions.

3.6. Mechanical properties

Fig. 5a–c show the Young's modulus (E), tensile strength (σ_t), and elongation at break (ε_b) of different bionanocomposite films. The values of E, σ_t and ε_b for A-F were 1260 ± 169 MPa, 46.8 ± 5.6 MPa, and 22.6 ± 4.6%, respectively [33]. In comparison, A/GO-F and A/rGO-F displayed higher E (1723 ± 59 MPa and 1489 ± 135 MPa, respectively) and higher σ_t (55.7 ± 1.0 MPa and 57.7 ± 1.1 MPa, respectively), confirming that GO and rGO reinforced the biopolymers. A/GO-F had lower ε_b (15.3 ± 3.6%) while A/rGO-F showed a ε_b value (20.0 ± 8.8%) similar to that of A-F. Clearly, the interactions between GO/rGO and chitosan

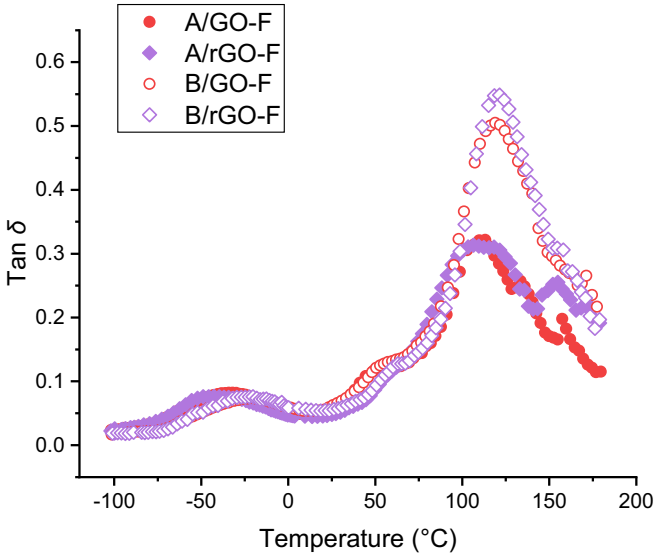

Fig. 4. DMTA curves for the different bionanocomposite films.

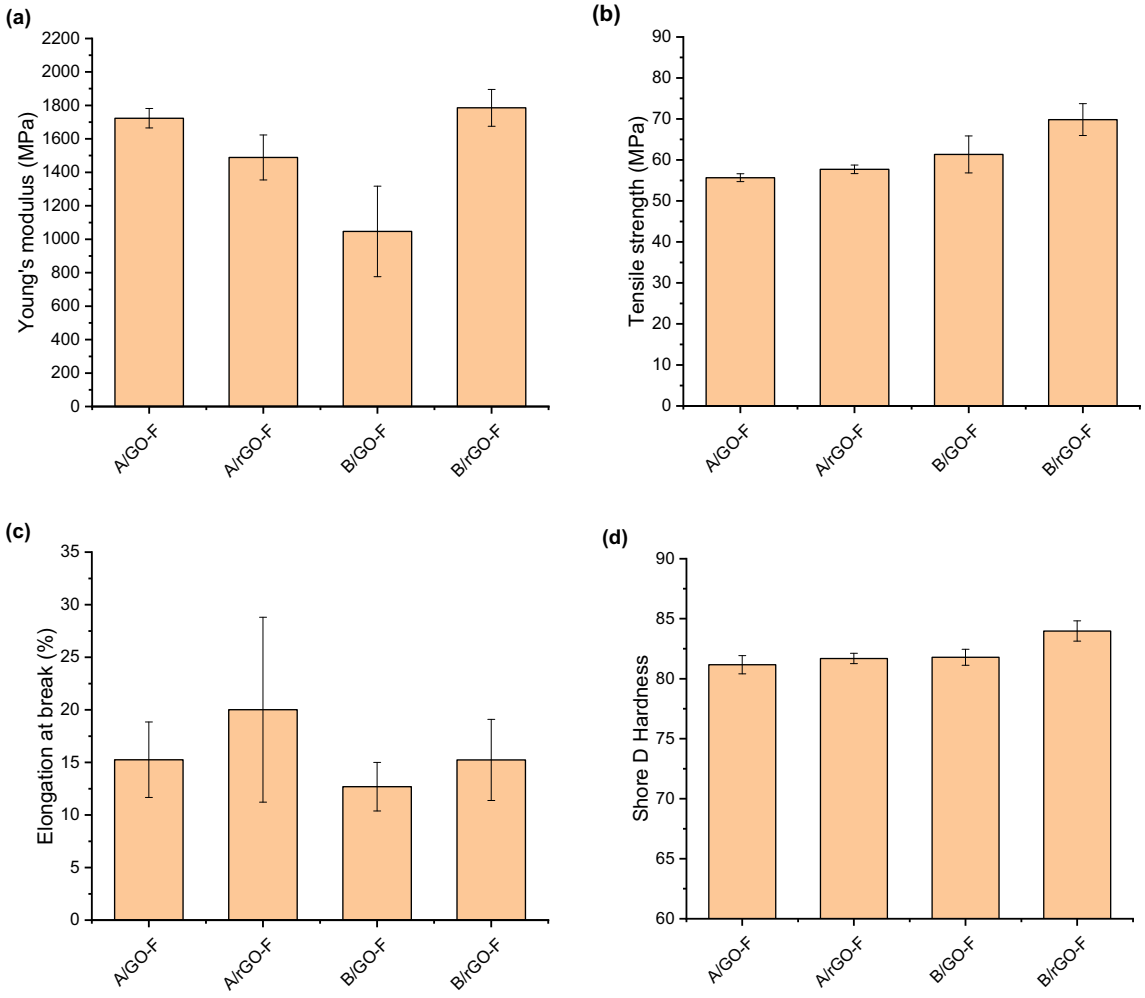

Fig. 5. Tensile (a, tensile strength; b, Young's modulus; and c, Elongation at break) and d) Shore D hardness of the different bionanocomposite films. Error bars represent standard deviations.

chains can lead to a mechanism for effective interfacial stress transfer. In this way, the well-dispersed GO/rGO in the chitosan matrix can facilitate uniform stress distribution and minimise the occurrence of stress concentration, leading to enhanced mechanical properties of the biopolymers [45,47]. Considering σ_t and ε_b, rGO seemed to give a greater reinforcement effect than GO, which additionally may be associated with higher crystallinity in A/rGO-F than in A/GO-F (see XRD results). Moreover, all the A-series of films showed a stress–strain curve typical of a hard and tough polymer, with strain hardening observed (see Fig. S5). This demonstrates the strong hydrogen-bonding interactions between biopolymer chains.

The values of E, σ_t and ε_b for B-F were 1325 ± 176 MPa, 50.5 ± 3.6 MPa, and 10.4 ± 3.4%, respectively [33]. B/GO-F had E = 1047 ± 270 MPa, σ_t = 61.3 ± 4.5 MPa, and ε_b = 12.7 ± 2.3% and, B/rGO-F had E = 1786 ± 110 MPa, σ_t = 69.8 ± 3.9 MPa, and ε_b = 15.2 ± 3.9%. In summary, rGO provided better reinforcement of the chitosan/CMC matrix as well. The σ_t of B/rGO-F was higher than all the other samples. Given this, both the PEC between chitosan and CMC and the stress transfer effect provided by rGO on the matrix could account for the enhanced mechanical properties. Additionally, for both B/GO-F and B/rGO-F, again, a stress–strain curve typical of a hard and tough polymer with strain hardening was obtained (see Fig. S5), confirming the presence of strong interactions between biopolymer chains.

Fig. 5d shows the Shore D hardness values of the different samples. The hardness values of A/GO-F, A/rGO-F, B/GO-F, and B/rGO-F were 81.2 ± 0.8, 82.7 ± 0.4, 81.8 ± 0.7, and 84.0 ± 0.9, which were apparently higher than that of A-F (77.2 ± 0.9) and B-F (77.5 ± 0.9) [33]. In particular, B/rGO-F had a Shore D hardness higher than those of all other films. These results, again, demonstrate the mechanical reinforcement achieved on inclusion of rGO, in agreement with the tensile testing data.

3.7. Thermal stability

The thermal stability of different biopolymer films was studied by TGA, with the derivative weight plots as a function of temperature shown in Fig. 6. For A/GO-F and A/rGO-F, there was a major weight loss between 240 °C and 375 °C, accompanied by a small, sharp peak between 198 °C and 240 °C attributed to the initial de-polymerisation of the biopolymer. Additionally, there was moderate weight loss between 60 °C and 198 °C, which was due to moisture loss. While these two A-samples showed very similar derivative-weight profiles as that for A-F [33], the effect of the GO/rGO addition was apparent. While A-F displayed a major peak temperature of 297 °C [33], this value decreased to 289 °C for A/GO-F and increased to 307 °C for A/rGO-F. GO decreased the thermal stability of chitosan, whereas rGO resulted in an apparent increase in the thermal stability of the matrix. The GO used in this study is relatively thermally unstable with the major mass loss occurring between about 150 and 240 °C peaking at 207 °C (Fig. S6), presumably due to pyrolysis of the labile oxygen-containing functional groups [57]. It is likely that the thermal sensitivity of these oxygen-containing functional groups of GO promoted the thermal decomposition of

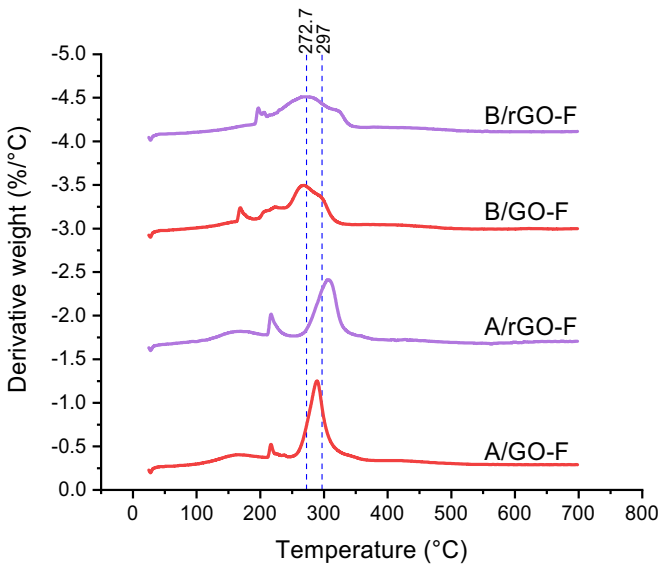

Fig. 6. Derivative-weight-loss curves for the different bionanocomposite films. The reference lines indicate the major peak temperatures of A-F (297 °C) and B-F (272.5 °C), respectively [33].

chitosan. In contrast, when much more stable rGO [57] was used, the well-dispersed nanosheets can hinder the diffusion of degradation products and, increase the activation energy for thermal degradation [58].

B-F had major weight loss of biopolymers as peaks overlapped at 273 °C and 306 °C, along with small peaks at 169 °C and 223 °C associated with the initial de-polymerisation of the biopolymers [33]. The overlapped peaks at the higher temperature (306 °C) may be attributed to the polyelectrolyte complexed structure of biopolymers that have higher thermal stability. For B/GO-F, two major derivative-weight peaks were at 269 °C and 297 °C, respectively. Thus, the addition of GO resulted in decreased biopolymer thermal stability which, again, may be associated with the oxygen-containing functional groups of GO. In contrast, when rGO was added, the characteristic peak for the complexed structure increased to about 322 °C, even higher than the major peak temperature for A/rGO-F. Clearly, the combined effects of PEC and the excellent dispersion of the more thermally-stable rGO results in enhanced matrix thermal stability.

3.8. Surface hydrophilicity

Fig. 7a shows bar charts of the change in θ_c values for the different bionanocomposite films, a measure of film surface hydrophilicity. Both θ_c values at 0 s and 60 s (θ_{c0s} and θ_{c60s}) were recorded, since θ_c changes after the drop of water is placed on the surface of the sample. The θ_{c0s} and θ_{c60s} of A-F were $90 \pm 5°$ and $68 \pm 5°$, respectively [33]. In comparison, for A/GO-F $\theta_{c0s} = 99 \pm 5°$ and $\theta_{c60s} = 88 \pm 4°$, the addition of GO to chitosan decreased the surface hydrophilicity. The combination of hydrogen-bonding and electrostatic interactions between chitosan and GO and the excellent dispersion of GO in chitosan may reduce the concentration of free hydroxyl groups and hinder interaction between the matrix and water. However, the presence of rGO in the chitosan system did not result in an increase in film surface hydrophobicity as for A/rGO-F $\theta_{c0s} = 84 \pm 8°$ and $\theta_{c60s} = 55 \pm 4°$. This result is unexpected considering rGO is less hydrophilic and contains less oxygen functional groups than GO. We propose that the reduced interaction between rGO and chitosan resulted in more free hydroxyl groups of chitosan and therefore, increased surface hydrophilicity.

For B-F $\theta_{c0s} = 71 \pm 6°$ and $\theta_{c60s} = 60 \pm 5°$, the film exhibited increased surface hydrophilicity due to the CMC sodium salt [33]. GO showed a positive effect, again, in reducing the surface hydrophilicity

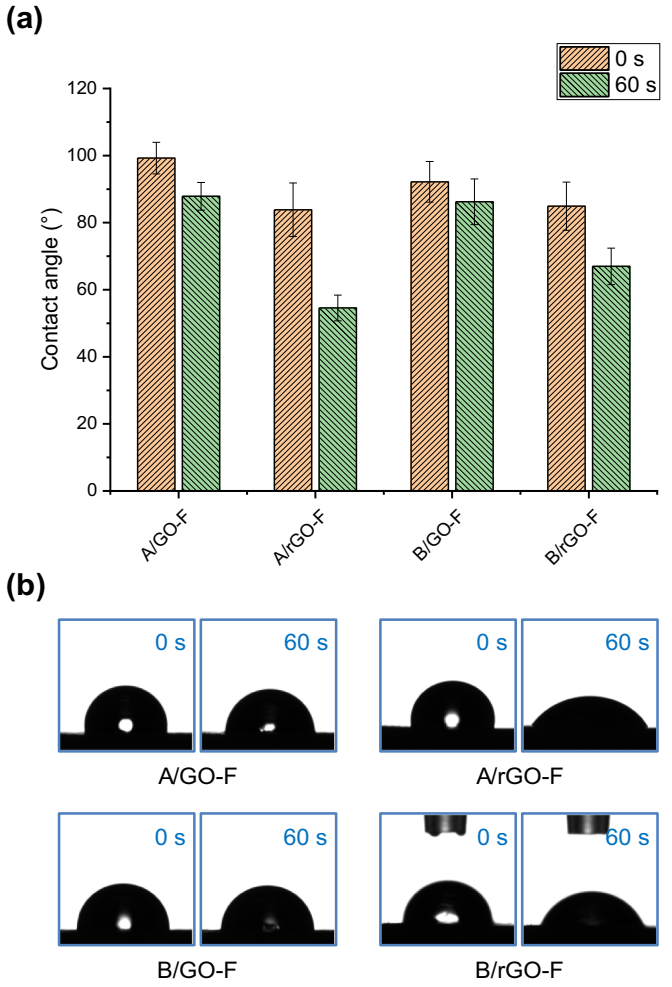

Fig. 7. a) Contact angle values and b) droplet images for the different bionanocomposite films at 0 s and 60 s. Error bars represent standard deviations.

of the chitosan/CMC matrix, with θ_{c0s} and θ_{c60s} of B/GO-F being $92 \pm 6°$ and $86 \pm 7°$, respectively. In this case, although PEC between chitosan and CMC was expected, there could still be some degree of interactions between chitosan and GO, reducing the availability of the biopolymer hydroxyl and carboxyl groups to bind with water. For B/rGO-F $\theta_{c0s} = 85 \pm 7°$ and $\theta_{c60s} = 67 \pm 6°$, indicating inclusion of rGO also increased the hydrophobicity of the chitosan/CMC matrix but not as effectively as GO did. In this instance, more free hydroxyl groups of biopolymers could be exposed responsible for surface hydrophilicity.

Based on the θ_c results, the surface hydrophilicity of the bionanocomposite films is predominately influenced by the chemical nature of the biopolymer matrix rather than that of the 2D graphene.

3.9. Electrochemical properties

EIS was employed to investigate the electrochemical properties of the different bionanocomposite films, see Fig. 8. The EIS data obtained was analysed by constructing Nyquist plots (Fig. 8a), which display a half semicircle at high-frequency, characteristic of a combination of bulk resistance and bulk capacitance in parallel, and an inclined line at the low frequency, which is associated with effects of the mixed electrode and electrolyte interface [59]. The intercept on the real axis gives the bulk resistance (R_b) [59]. Then, the conductivity (σ_{dc}) of the polymer electrolyte could be calculated using Eq. (7), with the relevant values listed in Table S3. It can be seen that A-F and A/rGO-F had similar σ_{dc} while that of A/GO-F was moderately lower. B-F had lower σ_{dc}, whereas the addition of GO or rGO led to higher σ_{dc}, with a greater

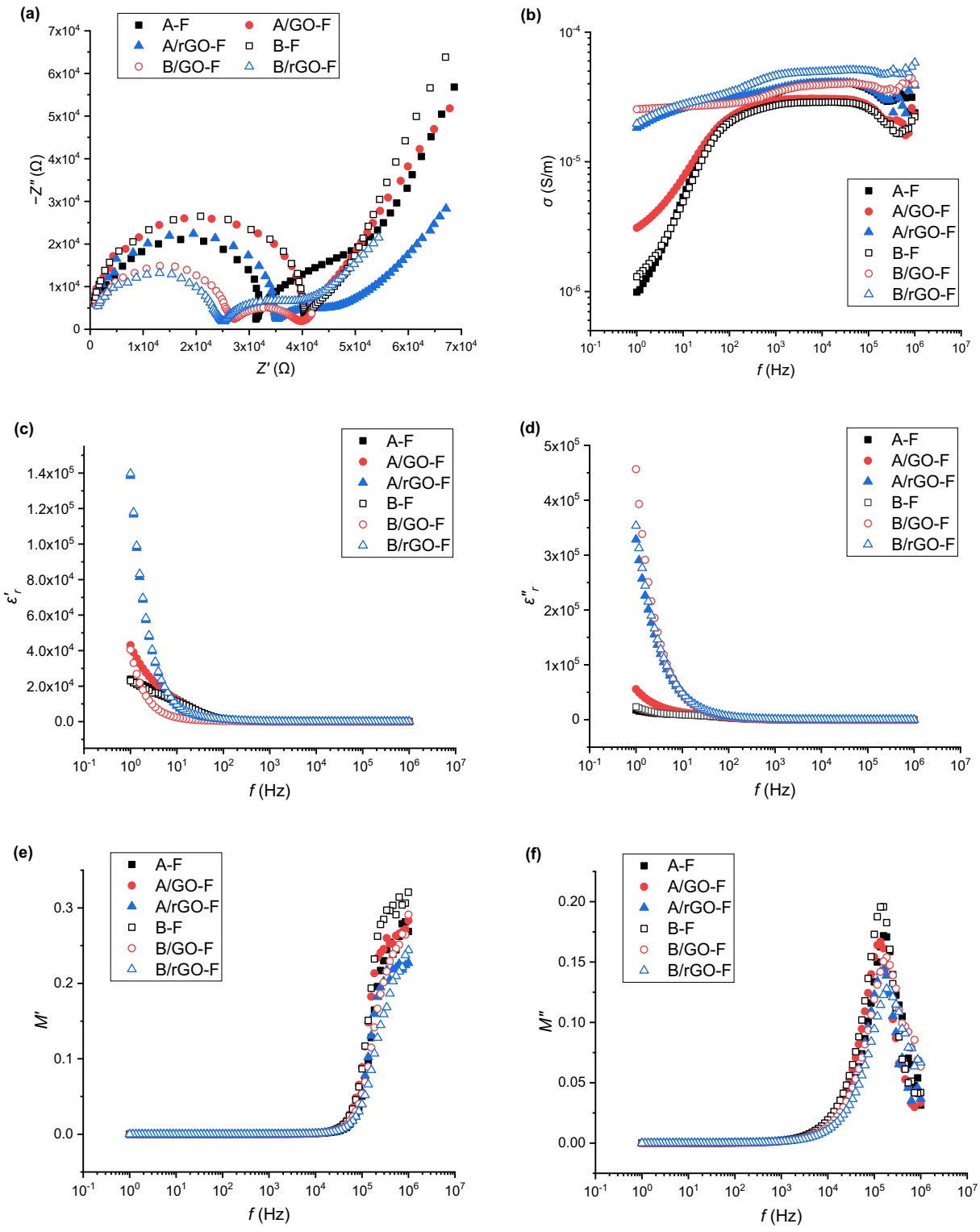

Fig. 8. EIS results for the different bionanocomposite films: a) Nyquist plot of impedance; b) AC conductivity (σ); c) real relative permittivity (ε'_r); d) imaginary relative permittivity (ε''_r); e) real electric modulus (M'); and f) imaginary electric modulus (M'').

increase by rGO. In this regard, the stronger hydrogen-bonding and/or electrostatic interactions between biopolymer chains in A/GO-F and B-F led to their lower σ_{dc} values, whereas the addition of rGO in the system led to reduced biopolymer chain interactions and higher σ_{dc}.

Fig. 8b is a plot of the change in AC conductivity (σ) as a function of frequency. For all the samples, σ increased with frequency, which is typical of an insulating material (dielectric). The low σ values could result from the accumulation of charged species at the electrode–electrolyte interface, leading to less mobile ions in the bulk material contributing towards conductivity [39]. For A-F, A/GO-F, and B-F at low frequency (<100 Hz), σ was particularly low (between 2×10^{-5} and 3×10^{-6} S/m) and sharply increased with frequency.

Fig. 8c and d shows that for all the samples, decreasing frequency led to both abrupt increases in both ε'_r and ε''_r. The high ε'_r and ε''_r values at

low frequencies indicate electrode polarisation and space charge effects (dipole moment). At high frequencies, the fast periodic reversal could inhibit charge accumulation and polarisation, which contributed to decreased ε'_r and ε''_r [60,61]. A/rGO-F and B/rGO-F displayed higher ε'_r than other samples at low frequencies (<10 Hz). Given this, electrically conductive rGO might have assisted the accumulation of mobile ions. Moreover, all the samples had relatively high ε'_r values (see Table S1). The highest ε'_r value at 1 kHz was displayed by A-F (152 ± 76) and the lowest by B-F (62 ± 17).

Fig. 8e and f show that M' had very low values at low frequencies, which can be attributed to the lack of restoring force for the electrical field-induced mobile ions (or, for the removal of electrode polarisation) [40,62]. At low frequencies, M'' also exhibited low values, which might be due to the large capacitance resulting from the accumulation of large amounts of charge carriers at the electrode–polymer electrolyte interface [40,63]. The increase in M' with increasing frequency can be considered to be due to relaxation. Correspondingly, M'' exhibited a well-defined peak at high frequencies, indicating relaxation processes with distributed relaxation times (*i.e.* viscoelastic relaxation, or dipolar relaxation) [42]. This peak also suggests that these materials were ionic conductors [42,60]. For the different bionanocomposite films, this relaxation peak occurred at a similar frequency, implying that the relaxation time was not affected by the addition of GO or rGO.

4. Conclusions

In this study, we have compared the effects of GO and rGO, the latter more hydrophilic than the former, on the properties of polyelectrolyte complexed biopolymer materials. While it is widely believed that nanofiller–matrix interactions are crucial for property enhancement in nanocomposites, our results unexpectedly show that inclusion of GO, which has a greater affinity with chitosan than rGO, did not always yield the most desirable composite properties. STEM images show that while our thermomechanical processing protocol enabled excellent dispersion of GO/rGO in either the chitosan or chitosan/CMC matrix, agglomerations of GO were present in B/GO-F, possibly attributed to the negatively charged CMC. Irrespective of the biopolymer matrix, rGO provided better mechanical reinforcement than GO. Given this, stronger interaction of GO with chitosan may disrupt the biopolymer interactions. Moreover, addition of rGO enhanced the biopolymer thermal stability. The similar increase in the α-transition temperature detected for B/GO-F and B/rGO-F demonstrated the constraint on biopolymer chain mobility was not determined only by the chemical nature of the nanofiller. Compared with rGO, GO was more effective at increasing the surface hydrophobicity of the biocomposite films, possibly due to the reduced availability of moisture-sensitive chemical groups of the biopolymers. Likewise, the electrochemical properties of the bionanocomposite films were more influenced by the interactions between the biopolymers than by GO/rGO. This new understanding can provide insights into the rational design of bionanocomposite materials with enhanced properties.

CRediT author statement

Pei Chen: Methodology, Validation, Formal Analysis, Investigation. **Fengwei Xie:** Conceptualization, Methodology, Validation, Formal analysis, Investigation, Resources, Data Curation, Writing - Original Draft, Writing - Review & Editing, Visualization, Supervision, Project administration, Funding acquisition. **Fengzai Tang:** Investigation, Writing - Original Draft. **Tony McNally:** Conceptualization, Resources, Writing - Review & Editing, Supervision, Funding acquisition.

Declaration of competing interest

None.

Acknowledgements

The authors acknowledge funding from the European Union's Horizon 2020 - Research and Innovation Framework Programme under the Marie Skłodowska-Curie grant agreement No. 798225. P. Chen acknowledges the financial support from the China Scholarship Council (CSC) for her visiting position and thanks IINM, WMG, University of Warwick, UK for hosting her research visit. F. Xie also acknowledges support from the Guangxi Key Laboratory for Polysaccharide Materials and Modification, Guangxi University for Nationalities, China (Grant No. GXPSMM18ZD-02).

Appendix A. Supplementary data

Supplementary data to this article can be found online at https://doi.org/10.1016/j.ijbiomac.2020.04.259.

References

[1] S.-B. Park, E. Lih, K.-S. Park, Y.K. Joung, D.K. Han, Biopolymer-based functional composites for medical applications, Prog. Polym. Sci. 68 (2017) 77–105.
[2] J. Chen, F. Xie, X. Li, L. Chen, Ionic liquids for the preparation of biopolymer materials for drug/gene delivery: a review, Green Chem. 20 (18) (2018) 4169–4200.
[3] S. Van Vlierberghe, P. Dubruel, E. Schacht, Biopolymer-based hydrogels as scaffolds for tissue engineering applications: a review, Biomacromolecules 12 (5) (2011) 1387–1408.
[4] W. Xu, X. Wang, N. Sandler, S. Willför, C. Xu, Three-dimensional printing of wood-derived biopolymers: a review focused on biomedical applications, ACS Sustain. Chem. Eng. 6 (5) (2018) 5663–5680.
[5] X. Lin, Y. Liu, A. Bai, H. Cai, Y. Bai, W. Jiang, H. Yang, X. Wang, L. Yang, N. Sun, H. Gao, A viscoelastic adhesive epicardial patch for treating myocardial infarction, Nat. Biomed. Eng. 3 (8) (2019) 632–643.
[6] A. Lee, A.R. Hudson, D.J. Shiwarski, J.W. Tashman, T.J. Hinton, S. Yerneni, J.M. Bliley, P.G. Campbell, A.W. Feinberg, 3D bioprinting of collagen to rebuild components of the human heart, Science 365 (6452) (2019) 482–487.
[7] D.S. Cha, M.S. Chinnan, Biopolymer-based antimicrobial packaging: a review, Crit. Rev. Food Sci. Nutr. 44 (4) (2004) 223–237.
[8] G. Cado, R. Aslam, L. Séon, T. Garnier, R. Fabre, A. Parat, A. Chassepot, J.C. Voegel, B. Senger, F. Schneider, Y. Frère, L. Jierry, P. Schaaf, H. Kerdjoudj, M.H. Metz-Boutigue, F. Boulmedais, Self-defensive biomaterial coating against bacteria and yeasts: polysaccharide multilayer film with embedded antimicrobial peptide, Adv. Funct. Mater. 23 (38) (2013) 4801–4809.
[9] J. Ma, Y. Sahai, Chitosan biopolymer for fuel cell applications, Carbohydr. Polym. 92 (2) (2013) 955–975.
[10] J.J. Koh, G.J.H. Lim, X. Zhou, X. Zhang, J. Ding, C. He, 3D-printed anti-fouling cellulose mesh for highly efficient oil/water separation applications, ACS Appl. Mater. Interfaces 11 (14) (2019) 13787–13795.
[11] S. Zhang, F. Lu, L. Tao, N. Liu, C. Gao, L. Feng, Y. Wei, Bio-inspired anti-oil-fouling chitosan-coated mesh for oil/water separation suitable for broad pH range and hyper-saline environments, ACS Appl. Mater. Interfaces 5 (22) (2013) 11971–11976.
[12] X. Zhou, F. Zhao, Y. Guo, B. Rosenberger, G. Yu, Architecting highly hydratable polymer networks to tune the water state for solar water purification, Sci. Adv. 5 (6) (2019), eaaw5484. .
[13] G. Chen, T. Li, C. Chen, C. Wang, Y. Liu, W. Kong, D. Liu, B. Jiang, S. He, Y. Kuang, L. Hu, A highly conductive cationic wood membrane, Adv. Funct. Mater. 29 (44) (2019), 1902772. .
[14] T. Jia, Y. Wang, Y. Dou, Y. Li, M. Jung de Andrade, R. Wang, S. Fang, J. Li, Z. Yu, R. Qiao, Z. Liu, Y. Cheng, Y. Su, M. Minary-Jolandan, R.H. Baughman, D. Qian, Z. Liu, Moisture sensitive smart yarns and textiles from self-balanced silk fiber muscles, Adv. Funct. Mater. 29 (18) (2019), 1808241. .
[15] R. Wang, S. Gao, Z. Yang, Y. Li, W. Chen, B. Wu, W. Wu, Engineered and laser-processed chitosan biopolymers for sustainable and biodegradable triboelectric power generation, Adv. Mater. 30 (11) (2018) 1706267.
[16] R. Xiong, A.M. Grant, R. Ma, S. Zhang, V.V. Tsukruk, Naturally-derived biopolymer nanocomposites: interfacial design, properties and emerging applications, Mater. Sci. Eng. R 125 (2018) 1–41.
[17] T. Kuilla, S. Bhadra, D. Yao, N.H. Kim, S. Bose, J.H. Lee, Recent advances in graphene based polymer composites, Prog. Polym. Sci. 35 (11) (2010) 1350–1375.
[18] J. Chen, H. Peng, X. Wang, F. Shao, Z. Yuan, H. Han, Graphene oxide exhibits broad-spectrum antimicrobial activity against bacterial phytopathogens and fungal conidia by intertwining and membrane perturbation, Nanoscale 6 (3) (2014) 1879–1889.
[19] F. Perreault, A.F. de Faria, S. Nejati, M. Elimelech, Antimicrobial properties of graphene oxide nanosheets: why size matters, ACS Nano 9 (7) (2015) 7226–7236.
[20] M. Di Giulio, R. Zappacosta, S. Di Lodovico, E. Di Campli, G. Siani, A. Fontana, L. Cellini, Antimicrobial and antibiofilm efficacy of graphene oxide against chronic wound microorganisms, Antimicrob. Agents Chemother. 62 (7) (2018), e00547-18. .
[21] A. Al-Jumaili, S. Alancherry, K. Bazaka, M.V. Jacob, Review on the antimicrobial properties of carbon nanostructures, Materials 10 (9) (2017), 1066. .

[22] S. Sayyar, E. Murray, B.C. Thompson, J. Chung, D.L. Officer, S. Gambhir, G.M. Spinks, G.G. Wallace, Processable conducting graphene/chitosan hydrogels for tissue engineering, J. Mater. Chem. A 3 (3) (2015) 481–490.
[23] A. Konwar, S. Kalita, J. Kotoky, D. Chowdhury, Chitosan–iron oxide coated graphene oxide nanocomposite hydrogel: a robust and soft antimicrobial biofilm, ACS Appl. Mater. Interfaces 8 (32) (2016) 20625–20634.
[24] S. Frindy, A. Primo, H. Ennajih, A. el kacem Qaiss, R. Bouhfid, M. Lahcini, E.M. Essassi, H. Garcia, A. El Kadib, Chitosan–graphene oxide films and CO2-dried porous aerogel microspheres: interfacial interplay and stability, Carbohydr. Polym. 167 (2017) 297–305.
[25] R. Justin, B. Chen, Characterisation and drug release performance of biodegradable chitosan–graphene oxide nanocomposites, Carbohydr. Polym. 103 (2014) 70–80.
[26] R. Wang, D. Shou, O. Lv, Y. Kong, L. Deng, J. Shen, pH-controlled drug delivery with hybrid aerogel of chitosan, carboxymethyl cellulose and graphene oxide as the carrier, Int. J. Biol. Macromol. 103 (2017) 248–253.
[27] Q. Wang, J.B. Schlenoff, The polyelectrolyte complex/coacervate continuum, Macromolecules 47 (9) (2014) 3108–3116.
[28] Y. Zhao, Y. Wu, L. Wang, M. Zhang, X. Chen, M. Liu, J. Fan, J. Liu, F. Zhou, Z. Wang, Bio-inspired reversible underwater adhesive, Nat. Commun. 8 (1) (2017), 2218. .
[29] Z. Li, H.R. Ramay, K.D. Hauch, D. Xiao, M. Zhang, Chitosan–alginate hybrid scaffolds for bone tissue engineering, Biomaterials 26 (18) (2005) 3919–3928.
[30] N. Iwasaki, S.-T. Yamane, T. Majima, Y. Kasahara, A. Minami, K. Harada, S. Nonaka, N. Maekawa, H. Tamura, S. Tokura, M. Shiono, K. Monde, S.-I. Nishimura, Feasibility of polysaccharide hybrid materials for scaffolds in cartilage tissue engineering: evaluation of chondrocyte adhesion to polyion complex fibers prepared from alginate and chitosan, Biomacromolecules 5 (3) (2004) 828–833.
[31] S. Basu, A. Plucinski, J.M. Catchmark, Sustainable barrier materials based on polysaccharide polyelectrolyte complexes, Green Chem. 19 (17) (2017) 4080–4092.
[32] C. Wei, X. Zhu, H. Peng, J. Chen, F. Zhang, Q. Zhao, Facile preparation of lignin-based underwater adhesives with improved performances, ACS Sustain. Chem. Eng. 7 (4) (2019) 4508–4514.
[33] P. Chen, F. Xie, F. Tang, T. McNally, Thermomechanical-induced polyelectrolyte complexation between chitosan and carboxymethyl cellulose enabling unexpected hydrolytic stability, Compos. Sci. Technol. 189 (2020), 108031. .
[34] V. Epure, M. Griffon, E. Pollet, L. Avérous, Structure and properties of glycerol-plasticized chitosan obtained by mechanical kneading, Carbohydr. Polym. 83 (2) (2011) 947–952.
[35] D.F. Xie, V.P. Martino, P. Sangwan, C. Way, G.A. Cash, E. Pollet, K.M. Dean, P.J. Halley, L. Avérous, Elaboration and properties of plasticised chitosan-based exfoliated nano-biocomposites, Polymer 54 (14) (2013) 3654–3662.
[36] C. Gao, E. Pollet, L. Avérous, Properties of glycerol-plasticized alginate films obtained by thermo-mechanical mixing, Food Hydrocoll. 63 (2017) 414–420.
[37] P. Chen, F. Xie, F. Tang, T. McNally, Competing interactions in dual-biopolymer nanocomposites, Compos. Sci. Technol. (2019) Submitted for publication.
[38] S.S. Abbas, G.J. Rees, N.L. Kelly, C.E.J. Dancer, J.V. Hanna, T. McNally, Facile silane functionalization of graphene oxide, Nanoscale 10 (34) (2018) 16231–16242.
[39] Z. Osman, Z.A. Ibrahim, A.K. Arof, Conductivity enhancement due to ion dissociation in plasticized chitosan based polymer electrolytes, Carbohydr. Polym. 44 (2) (2001) 167–173.
[40] A.S. Bhatt, D.K. Bhat, M.S. Santosh, C.-w. Tai, Chitosan/NiO nanocomposites: a potential new dielectric material, J. Mater. Chem. 21 (35) (2011) 13490–13497.
[41] R. Bowen Chris, S. Buschhorn, V. Adamaki, Manufacture and characterization of conductor-insulator composites based on carbon nanotubes and thermally reduced graphene oxide, Pure Appl. Chem. 86 (5) (2014) 765–774.
[42] I.A. Fadzallah, S.R. Majid, M.A. Careem, A.K. Arof, Relaxation process in chitosan–oxalic acid solid polymer electrolytes, Ionics 20 (7) (2014) 969–975.
[43] S. Park, J. An, J.R. Potts, A. Velamakanni, S. Murali, R.S. Ruoff, Hydrazine-reduction of graphite- and graphene oxide, Carbon 49 (9) (2011) 3019–3023.
[44] I.K. Moon, J. Lee, R.S. Ruoff, H. Lee, Reduced graphene oxide by chemical graphitization, Nat. Commun. 1 (1) (2010) 73.
[45] X. Yang, Y. Tu, L. Li, S. Shang, X.-m. Tao, Well-dispersed chitosan/graphene oxide nanocomposites, ACS Appl. Mater. Interfaces 2 (6) (2010) 1707–1713.
[46] D. Han, L. Yan, W. Chen, W. Li, Preparation of chitosan/graphene oxide composite film with enhanced mechanical strength in the wet state, Carbohydr. Polym. 83 (2) (2011) 653–658.
[47] Y. Pan, T. Wu, H. Bao, L. Li, Green fabrication of chitosan films reinforced with parallel aligned graphene oxide, Carbohydr. Polym. 83 (4) (2011) 1908–1915.
[48] G. Lawrie, I. Keen, B. Drew, A. Chandler-Temple, L. Rintoul, P. Fredericks, L. Grøndahl, Interactions between alginate and chitosan biopolymers characterized using FTIR and XPS, Biomacromolecules 8 (8) (2007) 2533–2541.
[49] A. Pawlak, M. Mucha, Thermogravimetric and FTIR studies of chitosan blends, Thermochim. Acta 396 (1) (2003) 153–166.
[50] Z. Chen, X. Mo, C. He, H. Wang, Intermolecular interactions in electrospun collagen–chitosan complex nanofibers, Carbohydr. Polym. 72 (3) (2008) 410–418.
[51] R.K. Layek, A. Kundu, A.K. Nandi, High-performance nanocomposites of sodium carboxymethylcellulose and graphene oxide, Macromol. Mater. Eng. 298 (11) (2013) 1166–1175.
[52] K. Shahzadi, I. Mohsin, L. Wu, X. Ge, Y. Jiang, H. Li, X. Mu, Bio-based artificial nacre with excellent mechanical and barrier properties realized by a facile in situ reduction and cross-linking reaction, ACS Nano 11 (1) (2017) 325–334.
[53] N. El Miri, K. Abdelouahdi, A. Barakat, M. Zahouily, A. Fihri, A. Solhy, M. El Achaby, Bio-nanocomposite films reinforced with cellulose nanocrystals: rheology of film-forming solutions, transparency, water vapor barrier and tensile properties of films, Carbohydr. Polym. 129 (0) (2015) 156–167.
[54] C. Rosca, M.I. Popa, G. Lisa, G.C. Chitanu, Interaction of chitosan with natural or synthetic anionic polyelectrolytes. 1. The chitosan–carboxymethylcellulose complex, Carbohydr. Polym. 62 (1) (2005) 35–41.
[55] I. Quijada-Garrido, B. Laterza, J.M. Mazón-Arechederra, J.M. Barrales-Rienda, Characteristic features of chitosan/glycerol blends dynamics, Macromol. Chem. Phys. 207 (19) (2006) 1742–1751.
[56] I. Quijada-Garrido, V. Iglesias-González, J.M. Mazón-Arechederra, J.M. Barrales-Rienda, The role played by the interactions of small molecules with chitosan and their transition temperatures. Glass-forming liquids: 1,2,3-Propantriol (glycerol), Carbohydr. Polym. 68 (1) (2007) 173–186.
[57] S. Stankovich, D.A. Dikin, R.D. Piner, K.A. Kohlhaas, A. Kleinhammes, Y. Jia, Y. Wu, S.T. Nguyen, R.S. Ruoff, Synthesis of graphene-based nanosheets via chemical reduction of exfoliated graphite oxide, Carbon 45 (7) (2007) 1558–1565.
[58] F. Xie, E. Pollet, P.J. Halley, L. Avérous, Starch-based nano-biocomposites, Prog. Polym. Sci. 38 (10—11) (2013) 1590–1628.
[59] N. Bonanos, B.C.H. Steele, E.P. Butler, Applications of impedance spectroscopy, in: E. Barsoukov, J.R. Macdonald (Eds.), Impedance Spectroscopy, John Wiley & Sons, Inc, Hoboken, NJ, USA 2005, pp. 205–537.
[60] A.S.A. Khiar, R. Puteh, A.K. Arof, Conductivity studies of a chitosan-based polymer electrolyte, Physica B 373 (1) (2006) 23–27.
[61] S. Navaratnam, K. Ramesh, S. Ramesh, A. Sanusi, W.J. Basirun, A.K. Arof, Transport mechanism studies of chitosan electrolyte systems, Electrochim. Acta 175 (2015) 68–73.
[62] A. Dutta, T.P. Sinha, P. Jena, S. Adak, Ac conductivity and dielectric relaxation in ionically conducting soda–lime–silicate glasses, J. Non-Cryst. Solids 354 (33) (2008) 3952–3957.
[63] L.N. Patro, K. Hariharan, Frequency dependent conduction characteristics of mechanochemically synthesized NaSn2F5, Mater. Sci. Eng. B 162 (3) (2009) 173–178.